PHYSICAL REVIEW RESEARCH **7**, 013046 (2025)

Measuring the angular momentum of a neutron using Earth's rotation

Niels Geerits[*] and Stephan Sponar
Atominstitut, Technische Universität Wien, Stadionallee 2, 1020 Vienna, Austria

Kyle E. Steffen and William M. Snow
Centre for Exploration of Energy and Matter, Indiana University, Bloomington, Indiana 47408, USA

Steven R. Parnell, Giacomo Mauri, Gregory N. Smith, and Robert M. Dalgliesh
ISIS, Rutherford Appleton Laboratory, Chilton, Oxfordshire OX11 0QX, United Kingdom

Victor de Haan
BonPhysics Research and Investigations BV, Laan van Heemstede 38, 3297AJ Puttershoek, Netherlands

(Received 19 July 2024; accepted 20 December 2024; published 13 January 2025)

A coupling between Earth's rotation and orbital angular momentum (OAM), known as the Sagnac effect, is observed in entangled neutrons produced using a spin-echo interferometer. After correction for instrument systematics the measured coupling is within 5% of theory, with an uncertainty of 7.2%. The OAM in our setup is transverse to the propagation direction and scales linearly with neutron wavelength (4–12.75 Å), so the Sagnac coupling can be varied without mechanically rotating the device, which avoids systematic errors present in previous experiments. The detected transverse OAM of our beam corresponds to $4098 \pm 295\ \hbar\text{Å}^{-1}$, 10^5 times lower than in the previous neutron experiments. This demonstrates the feasibility of using the Sagnac effect to definitively measure neutron OAM and paves the way towards a future observation of the quantum Sagnac effect.

DOI: 10.1103/PhysRevResearch.7.013046

I. INTRODUCTION

In noninertial frames of reference the laws of nature may appear to work differently, owing to additional quasi-forces that arise as a result of the nonuniform motion of the reference frame. George Sagnac's 1913 experiment is a famous example of such an effect. In an attempt to prove the existence of an ether, Sagnac observed a phase shift in his interferometer, which depended on the direction in which the interferometer was rotated [1]. The Sagnac effect manifests as an apparent coupling between the rotation frequency of the observer and the angular momentum of the test particle [2]. The famous 1925 experiment by Michelson, Gale, and Pearson, was able to observe this coupling in a very large optical interferometer owing to the Earth's rotation [3]. Since Sagnac and Michelson made their observations with light, the experimental question remained whether or not matter waves also experience a pseudopotential in a rotating frame. In 1965 the effect was first observed in superconducting electrons [4]. Then in 1979, Werner, Staudenmann, and Colella managed to demonstrate that free matter waves are also subject to the Sagnac effect. Specifically, neutrons traversing a rotating interferometer also experience a phase shift proportional to the inner product between the rotation frequency Ω and the orbital angular momentum (OAM) L spanned by the neutron's motion in the interferometer $(\Omega \cdot L)$ [5]. The rotation of the interferometer was realized by the natural rotation of the earth, as was the case in the 1925 Michelson/Gale/Pearson experiment. In addition to neutrons, the Sagnac effect has also been observed in other free matter waves, such as electrons [6] and atoms [7,8]. In 1988 Mashhoon demonstrated that applies to the total angular momentum

$$\hat{\mathbf{J}} = \hat{\mathbf{L}} + \hat{\mathbf{S}}, \tag{1}$$

therefore extending to the spin angular momentum $\hat{\mathbf{S}}$ of particles as well as their orbital angular momentum [9]. Recently, the Mashhoon effect has been observed in neutron polarimetry [10] and in neutron interferometry [11]. In these cases the rotating frame was realized by creating a rotating magnetic field in the laboratory frame of the interferometer, which, for the projective measurement of the neutron spin employed in the apparatus, can be shown to be equivalent to observing the neutron spin in a rotating frame of reference.

In parallel with this study on the Mashhoon effect, neutron researchers started to develop methods to produce neutrons with quantized OAM [12–15]. Neutron OAM would have several unique and/or applications within the fields of neutron scattering and quantum information. Examples of the former include probing multipole resonances in nuclear physics, which is currently being explored theoretically with photons

---

[*] Contact author: niels.geerits@tuwien.ac.at

[16], and unique scattering properties of twisted neutrons [17–19]. In addition the neutron nucleus weak interaction demonstrates a potential sensitivity to the total angular momentum possessed by the neutron [20]. Furthermore, as a quantum degree of freedom possessing infinite discrete levels, OAM may be a realistic candidate as for realizing qudits [21] with neutrons.

The mathematical form of quantum mechanical OAM is identical to the usual definition of angular momentum in the classical limit $\hat{L} = \hat{r} \times \hat{p}$, with the position and momentum promoted to operators. In addition, OAM distinguishes itself from its classical analog by existing only as discrete integer multiples of $\hbar$ upon measurement. Quantum OAM has various expressions in nature, ranging simply from frame-dependent "extrinsic" OAM, which is OAM that arises from the choice of reference frame, to frame-independent "intrinsic" OAM, such as orbitals of bound particles or the comparatively newer helical/twisted waves. OAM can be considered to be "intrinsic" if the expectation value of $\hat{L}$ is spatially translation invariant [22–24]. Later, we will demonstrate that both extrinsic and intrinsic OAM can be seen as a type of wave structure and that extrinsic states can be expressed as superpositions of intrinsic states. We will also show that extrinsic is not synonymous with not "quantum". Finally, we note that intrinsic and extrinsic OAM are parts of the same operator $\hat{L}$; hence, a potential, which depends on $\hat{L}$, does not discriminate between intrinsic and extrinsic OAM.

Detection of neutron OAM remains difficult and is the subject of debate and discussion in the scientific literature [25,26]. Current proposed methods are based on neutron scattering and absorption [17–19]. The simplicity of the effective potential created by the Sagnac effect, which contains only the OAM operator and an external quantity, could prove useful for the definitive detection of neutron OAM. The neutrons used in the 1975 experiment possessed OAM with respect to the center of the interferometer on the order of $10^9\hbar$. This OAM was detected by the rotation of the earth.

In this paper we present an experiment testing the feasibility of measuring OAM using the Sagnac effect. To this end a neutron interferometer with a precisely calibrated path separation was used. Since, this spatial separation and the neutron momentum are precisely known, it follows that the extrinsic transverse OAM carried by the neutrons is also precisely known. By measuring the resulting Sagnac phase we are able to determine the sensitivity of the setup to any transverse OAM, whether extrinsic or intrinsic. As noted previously, potentials depending on $\hat{L}$ do not discriminate between intrinsic and extrinsic OAM; hence, if our method successfully detects extrinsic OAM it will also detect intrinsic OAM and vice versa. Compared to the previous neutron Sagnac effect measurement, we improve the angular momentum sensitivity by five orders of magnitude. This improvement in sensitivity marks an important step towards observation of the quantized Sagnac effect. In optics this quantized Sagnac effect has been observed using spinning dove prisms [27]. The observation of a quantized energy shift from the Sagnac effect is an attractive method to resolve quantized OAM states in neutrons. We report on an experimental observation of the Sagnac effect in a neutron interferometer, which uses microscopic path separation on the order of the transverse coherence of the neutron (0.001–100 μm) [28–30]. In addition, we demonstrate that the Sagnac effect provides a good method for a basis to definitively detect the OAM of a particle. In the theory section we show that our setup not only produces the extrinsic transverse OAM, which we measure via the Sagnac effect, but also a much smaller intrinsic longitudinal OAM that may become accessible if sensitivity is improved. In the discussion section we propose to use rotating dove prisms to improve sensitivity such that this longitudinal OAM can be observed. Our experiment was carried out on the Larmor instrument at the ISIS pulsed neutron source. Larmor is a neutron spin-echo-type interferometer [31], which employs shaped RF spin flippers to induce horizontal spin- and energy-dependent path separation [32,33]. As a result the spin, energy, and path degrees of freedom of the neutron are entangled [34,35]. The latter had previously only been possible in perfect crystal neutron interferometry [36].

II. THEORY

In this section we distinguish between intrinsic and extrinsic OAM and attempt to express the latter in terms of the former. Next, we derive a formula for converting Cartesian position states into cylindrical (extrinsic) OAM states. Finally, we will explore the Sagnac effect in neutron spin-echo interferometry, SESANS. However, first we will start with some general definitions and properties of the OAM operator,

$$\hat{\mathbf{L}} = \hat{\mathbf{r}} \times \hat{\mathbf{p}}, \tag{2}$$

as shown in [37] in cylindrical coordinates we can focus on the z component since this is the only component that produces a nonzero expectation value,

$$\hat{L}_z = -\mathrm{i}\hbar\left(x\frac{\partial}{\partial y} - y\frac{\partial}{\partial x}\right) = -\mathrm{i}\hbar\frac{\partial}{\partial\phi}. \tag{3}$$

This operator has the eigenfunctions $e^{\mathrm{i}\ell\phi}$,

$$\hat{L}_z e^{\mathrm{i}\ell\phi} = \ell e^{\mathrm{i}\ell\phi}, \tag{4}$$

with ℓ, the OAM mode number, being integer. Since these vortex functions are also eigenfunctions of the free space Schrödinger equation in cylindrical coordinates, it follows that any free-space wavefunction can be written through superpositions of vortex modes,

$$\psi = \sum_\ell f^\ell(r,z)e^{\mathrm{i}\ell\phi}. \tag{5}$$

Using this knowledge we can define an OAM distribution function, a probability density function, telling us the chance of finding the wavefunction in the ℓth mode upon measurement,

$$p[\ell] = \frac{\int \mathrm{d}r\mathrm{d}z r|f^\ell(r,z)|^2}{\sum_\ell \int \mathrm{d}r\mathrm{d}z r|f^\ell(r,z)|^2}. \tag{6}$$

The nth moment of the OAM operator can be extracted simply from the OAM distribution function using the relation

$$\langle \hat{L}_z^n \rangle = \sum \ell^n p[\ell]. \tag{7}$$

For a variety of wavefunctions the first moment $n = 1$ (i.e., the expectation value) is spatially translation invariant. In this case one speaks of intrinsic OAM, which is further discussed in the next section.

A. Intrinsic and extrinsic OAM

Intrinsic OAM distinguishes itself from extrinsic OAM in that the former is invariant under frame translations. It has been shown in multiple publications [22–24] that this is the case if there is no propagation in the plane in which the OAM is defined. This plane is henceforth referred to as the x-y or r-ϕ plane (i.e., for OAM to be fully intrinsic we require $\langle k_x\rangle = \langle k_y\rangle = 0$). It can easily be shown that the eigenstates of the OAM operator in cylindrical coordinates satisfy this condition,

$$\langle k_x\rangle \propto \int \mathrm{d}\phi\, e^{-\mathrm{i}\ell\phi}\frac{\partial}{\partial x}e^{\mathrm{i}\ell\phi} \propto \int \mathrm{d}\phi\, \ell \sin(\phi) = 0, \tag{8a}$$

$$\langle k_y\rangle \propto \int \mathrm{d}\phi\, e^{-\mathrm{i}\ell\phi}\frac{\partial}{\partial y}e^{\mathrm{i}\ell\phi} \propto \int \mathrm{d}\phi\, \ell \cos(\phi) = 0, \tag{8b}$$

noting that $\frac{\partial}{\partial x} = \cos(\phi)\frac{\partial}{\partial r} - \frac{\sin(\phi)}{r}\frac{\partial}{\partial\phi}$ and $\frac{\partial}{\partial y} = \sin(\phi)\frac{\partial}{\partial r} + \frac{\cos(\phi)}{r}\frac{\partial}{\partial\phi}$. However, superpositions of eigenfunctions do not satisfy this condition,

$$\langle k_x\rangle \propto \int \mathrm{d}\phi \sum_{\ell,n} e^{-\mathrm{i}\ell\phi}\frac{\partial}{\partial x}e^{\mathrm{i}n\phi}, \tag{9a}$$

$$\langle k_y\rangle \propto \int \mathrm{d}\phi \sum_{\ell,n} e^{-\mathrm{i}\ell\phi}\frac{\partial}{\partial y}e^{\mathrm{i}n\phi}, \tag{9b}$$

which can be simplified to

$$\langle k_x\rangle \propto \int \mathrm{d}\phi\, \cos(\phi)\sum_{\ell,n} e^{-\mathrm{i}(\ell-n)\phi}, \tag{10a}$$

$$\langle k_y\rangle \propto \int \mathrm{d}\phi\, \sin(\phi)\sum_{\ell,n} e^{-\mathrm{i}(\ell-n)\phi}, \tag{10b}$$

which are not zero if $\ell - n = \pm 1$. This means that the OAM carried by a wavefunction that consists of a superposition of two or more vortex states with neighboring mode numbers is not entirely intrinsic. We argue that if a state carries extrinsic OAM, this does not necessarily imply that the state or its OAM is not "quantum". Take the states $\ell, \ell+1$ and $\ell+2$, each of which individually is regarded as a quantum state, the superposition of ℓ and $\ell+2$, carries only intrinsic OAM and is also considered a standard quantum mechanical state. It follows that superpositions that include $\ell+1$ are also "quantum" and carry extrinsic OAM.

Extrinsic OAM can emerge from superpositions of intrinsic states and vice versa as shown later. Extrinsic OAM mimics classical AM in that it is coordinate dependent and can be calculated as [37]

$$\langle \hat{\mathbf{L}}_{\text{ext}}\rangle = \langle\hat{\mathbf{r}}\rangle \times \langle\hat{\mathbf{p}}\rangle = \langle\hat{\mathbf{L}}\rangle - \langle\hat{\mathbf{L}}_{\text{int}}\rangle \tag{11}$$

as one would calculate classical AM. This sometimes leads to the erroneous claim that extrinsic OAM is not related to wave structure. This disregards the fact that both the expectation values $\langle\hat{\mathbf{r}}\rangle$ and $\langle\hat{\mathbf{p}}\rangle$ are related to the wave structure. We note that the second moment of the OAM operator

$$\hat{L}_z^2 = -\hbar^2\left(x^2\frac{\partial^2}{\partial y^2} + y^2\frac{\partial^2}{\partial x^2} - 2xy\frac{\partial}{\partial x}\frac{\partial}{\partial y} - y\frac{\partial}{\partial y} - x\frac{\partial}{\partial x}\right) \tag{12}$$

is not translation invariant. This can be demonstrated by taking the difference between $\hat{L}_z^2$ and a translated version $\hat{L}'^2_z$ (i.e., $x' \to x + x_0$ and $y' \to y + y_0$), which is given by

$$\Delta\hat{L}_z^2 = -\hbar^2\bigg(\left(x_0^2 - 2xx_0\right)\frac{\partial^2}{\partial y^2} + \left(y_0^2 - 2yy_0\right)\frac{\partial^2}{\partial x^2} + 2(xy_0 + yx_0)\frac{\partial}{\partial x}\frac{\partial}{\partial y} + y_0\frac{\partial}{\partial y} + x_0\frac{\partial}{\partial x}\bigg). \tag{13}$$

Each individual term needs to produce a zero expectation value if the second moment of $\hat{L}_z$ is to be translation invariant. For the eigenfunctions of $\hat{L}_z$ it can be easily shown that the momentum spread operators $\propto \frac{\partial^2}{\partial x^2}$ and $\propto \frac{\partial^2}{\partial y^2}$ produce a nonzero expectation value. For example,

$$\left\langle\hat{p}_x^2\right\rangle = -\int \mathrm{d}\phi e^{-\mathrm{i}\ell\phi}\frac{\partial^2}{\partial x^2}e^{\mathrm{i}\ell\phi} = \pi\ell^2. \tag{14}$$

It follows that the second moment of the OAM operator is not translation invariant, meaning that the OAM distribution function [Eq. (6)] changes when viewing the wavefunction in another frame of reference. We underline the importance of this fact, since many OAM-dependent interactions, such as scattering and absorption of twisted neutrons [17–19] do not depend on the expectation value $\langle\hat{L}_z\rangle$ but rather on the amplitude of the respective mode number. We contrast this with the method described in this paper, which measures the difference between the OAM expectation values of two states. We now examine wavefunctions with extrinsic OAM, and attempt to demonstrate that these can be seen as "partial" vortex states. We start from a wavefunction with purely extrinsic OAM: a planewave with Gaussian envelope propagating offset from the cylinder axis, by δ (z axis) in the x-y plane

$$\psi_t = Ae^{-\frac{(x-\delta)^2}{\sigma^2} - \frac{y^2}{\sigma^2}}e^{ik_y y}, \tag{15}$$

σ denotes the coherence length [28,30] of the wavepacket. It is clear that the total and extrinsic OAM are equal and transverse to the propagation direction

$$\langle\psi_t|\hat{L}_z|\psi_t\rangle = \langle\psi_t|\hat{L}_{z,\text{ext}}|\psi_t\rangle = \hbar\delta k_y\hat{z}. \tag{16}$$

It follows that the intrinsic OAM component is zero. As stated earlier vortex modes form a complete basis; hence, we can expand (15) in terms of vortex states. This can be done using the Jacobi-Anger expansion [38],

$$\psi_t = Ae^{-\frac{r^2+\delta^2}{\sigma}}\sum_{m,n}\mathrm{i}^m J_m\left(-2\mathrm{i}\frac{\delta r}{\sigma^2}\right)J_n(k_y r)e^{\mathrm{i}(m+n)\phi}. \tag{17}$$

The ℓth mode of this wavefunction is therefore given by

$$\psi_t^\ell(r) = Ae^{-\frac{r^2+\delta^2}{\sigma^2}}\sum_m \mathrm{i}^m J_m\left(-2\mathrm{i}\frac{\delta r}{\sigma^2}\right)J_{\ell-m}(k_y r), \tag{18}$$

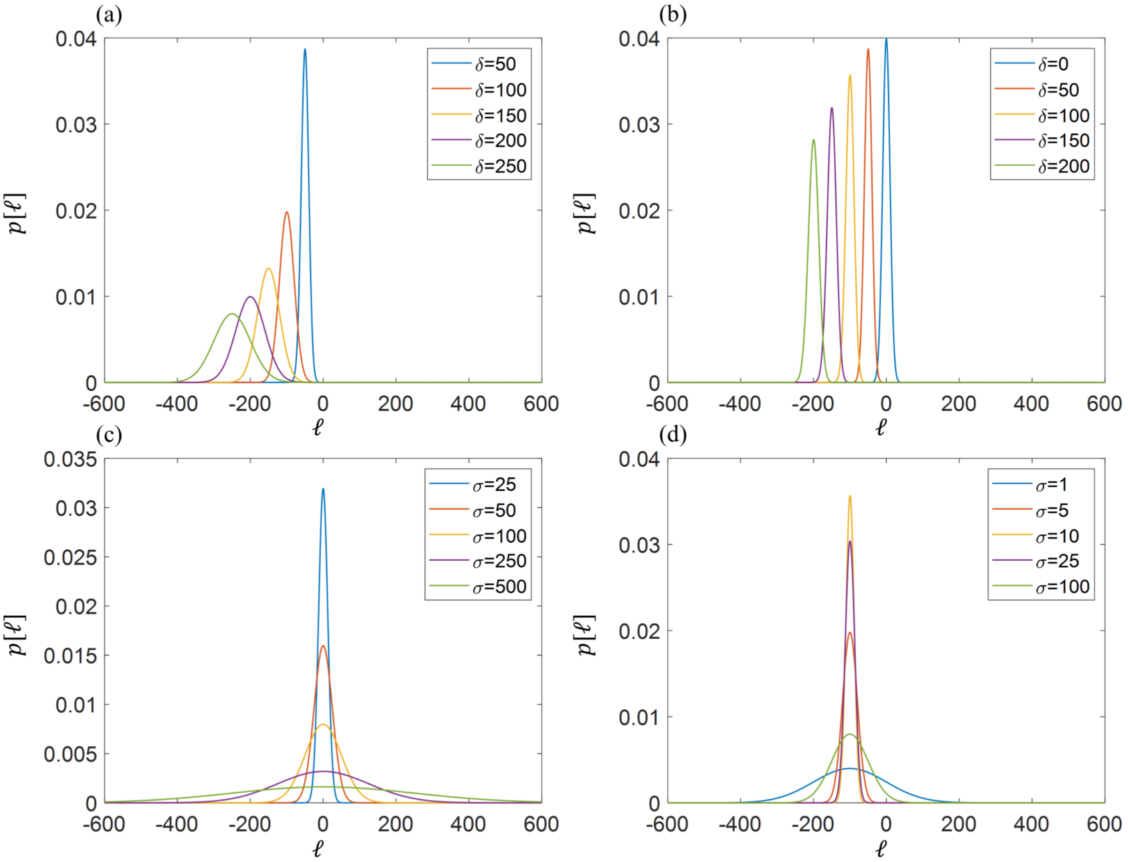

FIG. 1. OAM distribution function of a planewave with a Gaussian envelope according to Eq. (20) for various coherence lengths σ and offsets from the cylinder axis δ. In insets (a) and (b) the coherence length is fixed at 5 and 20, respectively, while in (c) and (d) δ has been fixed at 0 and 100, respectively. The momentum k_y is -1 in all cases.

which can be simplified using Grafs addition theorem for Bessel functions [39]

$$\psi_t^\ell(r) = Ae^{-\frac{r^2+\delta^2}{\sigma^2}} e^{\mathrm{i}\ell\alpha} J_\ell(k'r) \tag{19}$$

with $k' = \sqrt{k_y^2 - 4\frac{\delta^2}{\sigma^4}}$ and $\alpha = \sin^{-1}(-2\mathrm{i}\delta/\sigma^2 k') = \cos^{-1}(k_y/k')$. Equation (19) tells us which vortex states ψ_t^ℓ, each individually carrying intrinsic OAM, make up the Gaussian planewave carrying exclusively extrinsic OAM. Finally, the OAM distribution function can be determined according to Eq. (6), which becomes a standard Hankel transform given in [40] with the result

$$p[\ell] = \frac{A^2\sigma^2}{4} e^{\mathrm{i}\ell(\alpha-\alpha^*)} e^{-\frac{\sigma^2 k'^2}{4} - \frac{2\delta^2}{\sigma^2}} I_\ell\left(\frac{\sigma^2|k'|^2}{4}\right). \tag{20}$$

For the sake of illustration $p[\ell]$ is shown for a few combinations of σ and δ in Fig. 1. One can see that the central mode is always given by $\ell \approx k_y\delta$ as expected and that point like particles far away from the cylinder axis (i.e., particles with short coherence lengths and $\delta > \sigma$) have large OAM spreads. For illustration in Fig. 2 we compare the main cylinder mode of a Gaussian planewave given in Eq. (19) with the Gaussian planewave. While Fig. 1 shows clearly that many vortex modes can be used to construct a wavefunction with extrinsic OAM, Fig. 2 demonstrates that the inverse is also possible. Using a superposition of Gaussian planewaves carrying extrinsic OAM one could approximate the vortex state shown in Fig. 2. Or vice versa, by sampling only a small part of the vortex beam, with intrinsic OAM, we obtain a Gaussian planewave, which carries extrinsic transverse OAM. This sampling issue is explored in more detail in [41]. Most importantly both figures demonstrate qualitatively what we have previously quantitatively derived, extrinsic OAM can be seen as emerging from the wave structure of many intrinsic vortex states and vice versa. Finally, we wish to underline the key points to take away from this section: (i) intrinsic and extrinsic OAM are intricately related, such that they can be converted into each other, (ii) both extrinsic and intrinsic OAM can be understood as quantum phenomena, and (iii) if the reference frame is fixed, both extrinsic and intrinsic OAM will produce the same observable phenomena.

B. The Sagnac effect in SESANS

In this section, we derive the wavefunction produced by a SESANS-type interferometer, determine its OAM, and explore how the Sagnac effect couples to this OAM. In a rotating frame of reference, particles experience a pseudopotential proportional to the rotation rate of the frame and the OAM possessed by the particle around the axis of rotation,

$$\hat{V} \propto \Omega \cdot \hat{L}. \tag{21}$$

Intuitively, such a potential allows us to measure the OAM component of a wavefunction parallel to the axis of rotation.

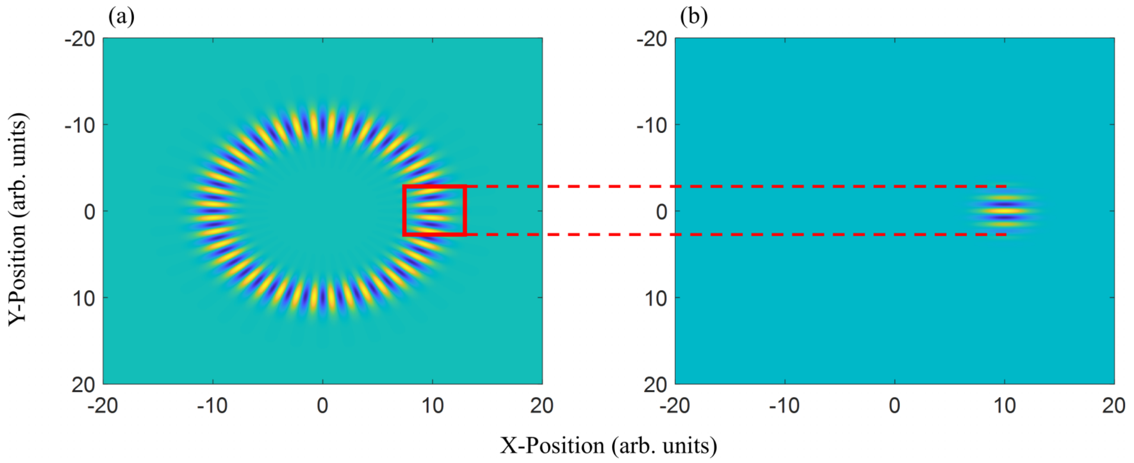

FIG. 2. Comparison of the real part of a planewave with a Gaussian envelope as described in Eq. (15), with $k_y = 4$, $\delta = 10$, and $\sigma = 2$ (b) and the main vortex mode ($\ell = 40$) contributing to the Gaussian planewave according to Eq. (19) (a). A red rectangle indicates the similarity between the vortex state and the offset Gaussian planewave.

Our setup is shown in Fig. 3. It is clear that the wavefunction of each spin state can be approximated by the Gaussian planewave we used previously to explore extrinsic OAM [Eq. (15)],

$$\psi_\pm = \frac{A}{\sqrt{2}} e^{\pm i\beta/2} e^{-\frac{(x\pm\delta_{SE}/2)^2 - y^2 - z^2}{\sigma^2}} e^{ik_y y}. \tag{22}$$

The z component has been added to the expression so that we can later also analyze the longitudinal OAM of this wavefunction. The $\pm$ refers to the spin state either being aligned with the z axis $+$ or anti-aligned $-$. β is an arbitrary phase between the up and down spin state. As shown previously the average OAM mode transverse to the propagation direction is

$$\ell_\pm = \pm\frac{\delta_{SE}|k|}{2}. \tag{23}$$

Usually the state in the interferometer is expressed as a spin-path entangled state. The path states are often characterized by the spin-echo length δ_{SE}. As we have seen this degree of freedom also characterizes the transverse OAM of the wavefunction. It follows that the two path states, defined by the spin-echo length, can also be described by two OAM states. Thus, for the purposes of this experiment, we describe our state not as spin-path entangled, but as spin-orbit entangled, such that the state in the interferometer can be described as

$$|\psi\rangle = e^{i\beta/2}|\ell_+\rangle|+\rangle + e^{-i\beta/2}|\ell_-\rangle|-\rangle \tag{24}$$

We note that state preparation and measurement are not instantaneous. Between the first and second RF flipper, spin-echo length and therefore transverse OAM is linearly increased, while between the third and fourth RF flipper, the spin-echo length and transverse OAM are reduced back to zero. The Sagnac effect will obviously also act on these intermediate states. This is taken into account by allowing for an OAM, which depends on the y coordinate. The precession frequency between the two states owing to the Sagnac effect follows from Eqs. (21) and (23) and is given by

$$\delta\omega_s = [\ell_+ - \ell_-]\Omega\sin(\Lambda), \tag{25}$$

with Λ the latitude of the interferometer. This expression demonstrates one of the advantages of using the Sagnac effect to measure OAM: the precession frequency depends only on the OAM difference between the two states. This difference is invariant under spatial translations of the frame of reference and, hence, intrinsicality/extrinsicality becomes an irrelevant detail. Integrating this precession frequency over the length of

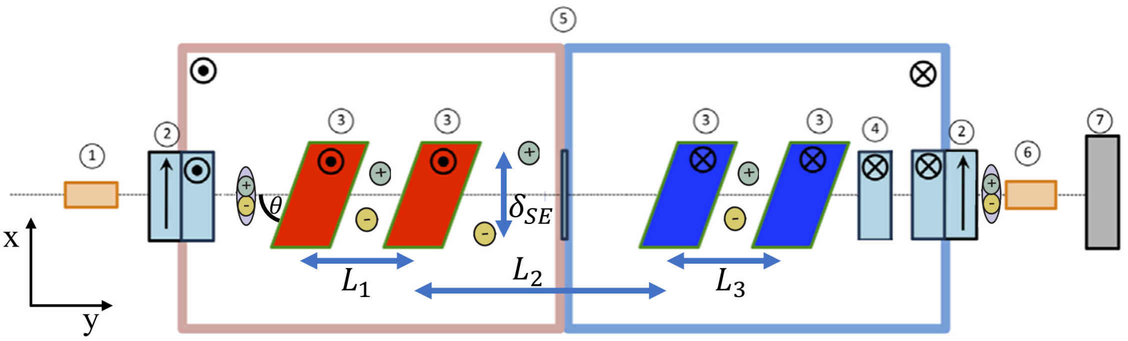

FIG. 3. Schematic of the Larmor neutron spin-echo interferometer, the propagation of the + and–spin through the device and the neutron optical components: (1) polarizer, (2) adiabatic $\pi/2$ rotator (v coil), (3) RF spin flipper with tilted field region, (4) ramped $\pi/2$ rotator, (5) guide field, (6) spin analyzer, and (7) detector.

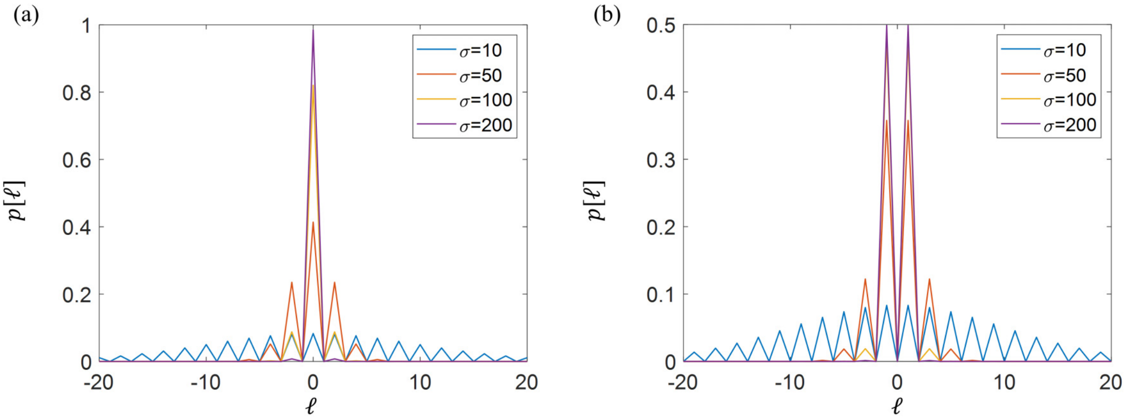

FIG. 4. OAM distribution functions describing the longitudinal vortex modes carried by the wavefunction Eq. (29) in the cases: (a) $\beta = 0$, where only even vortex modes contribute; and (b) $\beta = \pi$, where only odd vortex modes contribute, for various coherence lengths σ. The separation parameter is kept constant at $\delta = 100$. As the coherence length increases relative to the separation constant, the number of contributing higher-order modes decreases, until the limiting case where only the lowest-order modes play a role (i.e., for $\beta = 0$ $\ell = 0$ and for $\beta = \pi$ $\ell = \pm 1$.

the instrument leads to the Sagnac phase shift

$$\delta\phi_s = \int dt\ \delta\omega_s = \frac{m\Omega\Delta\ell}{\hbar|k|}\sin(\Lambda)[L_1 + L_3 + 2L_2], \tag{26}$$

which can be reduced to the result shown in [5,42] for a horizontal interferometer

$$\delta\phi_s = \frac{2mA\Omega}{\hbar}\sin(\Lambda), \tag{27}$$

with A the area spanned by the two paths of the interferometer. The area, illustrated in Fig. 3, is given by

$$A = \delta_{SE}\left[\frac{L_1 + L_3}{2} + L_2\right]. \tag{28}$$

As will be shown in the next section the spin-echo length δ_{SE} is proportional to wavelength squared in spin-echo interferometers. Hence, to vary the area of the interferometer and, therefore, the strength of the Sagnac effect, we may simply vary the wavelength of incident neutrons, whereas the 1979 perfect crystal experiment required physical rotation of the interferometer, which may induce systematic errors. We now characterize the longitudinal and intrinsic OAM of the wavefunction produced in a spin-echo interferometer. The most interesting case to look at is when the wavefunction [Eq. (22)] is postselected such that spin information is erased. We will look only at the transverse part of the wavefunction since only this is relevant to the longitudinal OAM,

$$\psi_T = \frac{A}{\sqrt{2}}\left[e^{i\beta/2}e^{-\frac{(x+\delta_{SE}/2)^2 - z^2}{\sigma^2}} + e^{-i\beta/2}e^{-\frac{(x-\delta_{SE}/2)^2 - z^2}{\sigma^2}}\right]. \tag{29}$$

We wish to derive the individual vortex modes, equivalent to Eq. (19), in the longitudinal direction and the respective OAM distribution function. This is relatively simple if we realize that both terms in Eq. (29) are translated versions of the wavefunction (15) in the special case where $k_y = 0$. Hence, we can reuse our results Eqs. (19) and (20) to characterize longitudinal OAM of the wavefunction Eq. (29). The vortex modes are given by

$$\psi^{\ell}_{t,2}(r) = \sqrt{2}Ae^{-\frac{r^2+\delta^2}{\sigma^2}}J_\ell(k'r)\cos(\ell\alpha + \beta/2) \tag{30}$$

and the OAM distribution function is given by

$$p[\ell] = \frac{A^2\sigma^2}{2}e^{-\frac{\sigma^2 k'^2}{4} - \frac{2\delta^2}{\sigma^2}}I_\ell\left(\frac{\sigma^2|k'|^2}{4}\right)|\cos|^2(\ell\alpha + \beta/2) \tag{31}$$

with $\delta = \delta_{SE}/2$, $k' = 2i\frac{\delta}{\sigma^2}$, and $\alpha = \pi/2$. The most interesting cases occur when $\beta = 0$, in which case all odd vortex modes are eliminated and $\beta = \pi$, where all even modes are eliminated. A few plots of Eq. (31) are shown in Fig. 4, for $\beta = 0$ and $\beta = \pi$ and various coherence lengths σ, the splitting parameter δ is left constant. One can see that once σ exceeds δ, that is to say if the splitting parameter is much smaller than the coherence length, only the lowest-order vortex modes contribute to the overall wavefunction. This is particularly interesting in the $\beta = \pi$ case, since for $\delta < \sigma$, the state approximates a superposition of $\ell = 1$ and $\ell = -1$. In analogy to spin optics we refer to such a state as a linearly polarized OAM state, since it consists of an equal superposition of the clockwise and counterclockwise rotating states. As shown earlier such a state carries intrinsic OAM, as the mode numbers are not neighbors. Although the OAM expectation value of such a state is zero, it distinguishes itself from the $\ell = 0$ state, as in theory it produces a nonzero Sagnac phase, given sufficient measurement resolution and is expected to interact differently with matter [17–19]. Since current measurement resolution is insufficient, this paper is only concerned with observing the Sagnac effect owing to the transverse extrinsic OAM of the wavefunction.

In Eq. (26) we put the acquired Sagnac phase in a form that shows that one can extract the difference between the quantum numbers for two OAM states, assuming instrument parameters and the rotation rate are well known. Hence, using the Sagnac effect can be a good relative measure to determine the OAM of a beam.

III. METHODS

Our measurements were carried out on the Larmor instrument at the ISIS pulsed neutron source [43]. Larmor is a SANS instrument with a versatile neutron resonant spin-echo toolbox, based on four gradient radio frequency spin flippers with shaped poleshoes, capable of performing inelastic techniques such as modulated intensity emerging from Zero effort (MIEZE) [33] and spin-echo (modulated) small angle neutron scattering [SE(M)SANS] [34,35,44,45]. Our experiment makes use of the SESANS mode of the instrument, which employs magnetic refraction from a tilted field region to induce spin-dependent spatial splitting and a second oppositely polarized field region to recombine the two split states (see Fig. 3). The path separation, also known as the spin-echo length, is proportional to the wavelength squared

$$\delta_{SE} = \frac{m\gamma B_0 L_1 \cot(\theta)}{2\pi^2\hbar}\lambda^2 = c_{SE}\lambda^2 \tag{32}$$

with γ the gyromagnetic ratio of the neutron, λ the neutron wavelength, m the neutron mass, B_0 the magnitude of the static magnetic field inside the RF flippers, and θ the angle between the incident beam and the magnetic field region. The constant c_{SE}, which summarizes all instrument parameters and constants, is called the spin-echo constant. This interferometric technique has previously been used to revisit the Colella-Overhauser-Werner experiment [42], put limits on exotic spin-gravity couplings [46] and measure Bell inequalities with neutrons [34,35].

Since Larmor uses spin-dependent refraction to realize the interferometer, the path and spin states of the neutron are coupled (i.e., mode entangled). Hence, any path-dependent phase shift is projected onto the spin and vice versa. As pointed out previously the path and OAM degree of freedom are related and, hence, the path state and also path phases, may also be described as orbit states/phases. In SESANS the spin is usually prepared, along the x axis, orthogonal to the beam propagation and B_0 direction. The expectation value of the spin, also called polarization, is usually also measured along the x direction, leading to a polarization of

$$P_x = P_0 \cos(\Delta\phi(\lambda)), \tag{33}$$

with $P_0 = \sqrt{P_x^2 + P_y^2 + P_z^2}$ and $\Delta\phi(\lambda)$ a polynomial in λ,

$$\Delta\phi(\lambda) = a_0 + a_1\lambda + a_2\lambda^2 + O(\lambda^3). \tag{34}$$

One may independently control the a_0 term by means of a ramped precession field, with $B(t) \propto 1/t$, which ensures that the spin of each wavelength on a ToF source is rotated by the same angle [47,48]. By setting a_0 equal to $\pi/2$ we effectively change the measurement direction to along the y axis, the propagation direction. Hence, the measured polarization becomes

$$P_y = P_0 \sin(\Delta\phi'(\lambda)), \tag{35}$$

which for small $\Delta\phi'$ may be linearized. For more details on the pre- and postselection in SESANS-type interferometers we refer to [49]. To remove the scaling factor P_0, we may normalize P_y by P_x. This normalized polarization still has a simple and accurate linearization for small $\Delta\phi$,

$$\frac{P_y}{P_x} \approx \epsilon + a_1\lambda + a_2\lambda^2, \tag{36}$$

with ϵ any imprecision in the quality of the $\pi/2$ rotation provided by the ramped precession field. We can estimate the second-order parameter, owing to the Sagnac effect using Eqs. (27) and (32),

$$a_2 = c_{SE}\frac{m\Omega}{\hbar}\sin(\Lambda)[L_1 + L_3 + 2L_2]. \tag{37}$$

However, additional perturbations arising from imperfections in the instrument can occur, which can affect the magnitude of the second-order term. Most notably a slight change in the precession plane can occur if an imperfect spin-optical component introduces an unintended low-probability spin flip. Components that may be suspected to introduce such an effect are primarily those which use adiabatic field changes to effect a spin rotation, e.g., v coils (item 2 in Fig. 3) and adiabatic RF flippers (item 3 in Fig. 3), since adiabatic spin-flip probabilities in both of these components can be described as

$$\rho \approx A_i\lambda^2\cos^2(k_i\lambda + \alpha), \tag{38}$$

assuming only slight imperfection [50,51] (i.e., low spin-flip probability). As a result, the precession plane will appear to oscillate with an amplitude proportional to λ^2 and in addition this effect will produce an abberation on a_2, since the $\cos^2$ component in Eq. (38) produces a constant offset $[A\cos^2(x) = A/2(1 + \cos(2x))]$. This offset can, of course, be isolated and subtracted from a_2, by measuring the amplitude of the precession plane oscillation. Since this effect is small it has not been relevant to measurements conducted with Larmor before; however, our experiment has sufficient sensitivity to uncover this systematic.

Measurements of the Sagnac phase were conducted using a poleshoe angle of $\theta = 40$ degrees and at an RF frequency of 2 MHz corresponding to a magnetic field strength of 68.6 mT. These consisted of polarization measurements with the ramped $\pi/2$ rotator turned off and on with both polarities (corresponding to a $\pi/2$ or $-\pi/2$ rotation). In addition, with the ramped $\pi/2$ rotator turned off a calibration measurement was carried out, in which a 2-micron silicon grating was inserted into the sample position of the instrument. The resulting correlation function, shown in Fig. 5(a), allows us to experimentally determine the proportionality constant between the spin-echo length and the wavelength squared, which is essential to estimate a_2. Since the nth peak in Fig. 5(a) corresponds to a spin-echo length of n times the grating period, one can extract the relationship between spin-echo length and wavelength, shown in Fig. 5(b). By applying a quadratic fit one finds the spin-echo constant c_{SE} to be equal to $0.137\ \mu\text{m}\,\text{Å}^{-2}$. Using this and Eq. (37) it follows that for the instrument settings used in this experiment, the Sagnac constant a_2 should be equal to $-1.15 \times 10^{-3}\ \text{Å}^{-2}$. Equations (23) or (26) show that the difference between OAM states scales linearly with λ (i.e., $\delta\ell = c_{\text{OAM}}\lambda$). Using Eq. (26) we can express c_{OAM} in terms of a_2,

$$c_{\text{OAM}} = \frac{2\pi\hbar a_2}{m\Omega\sin(\Lambda)[L_1 + L_3 + 2L_2]}, \tag{39}$$

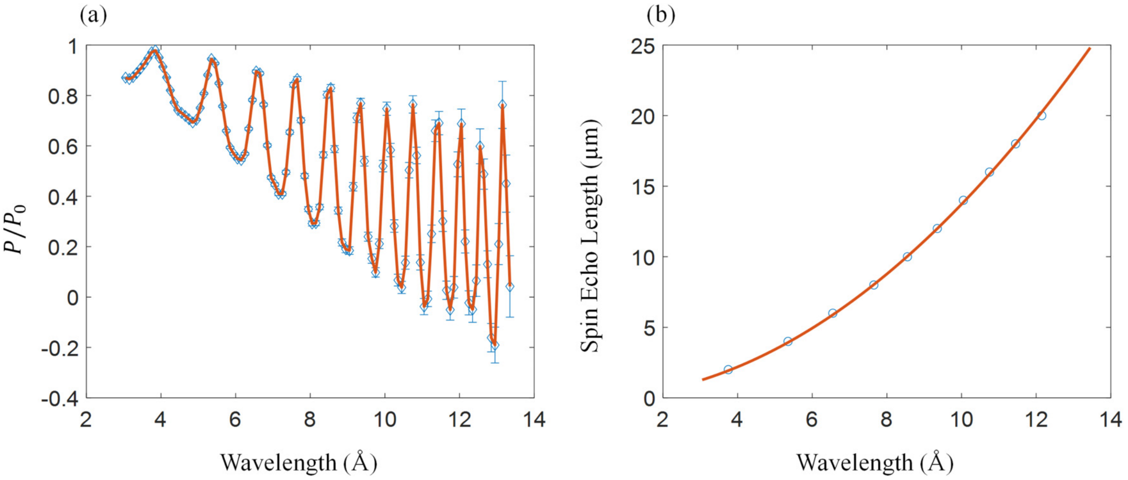

FIG. 5. Calibration curves of the instrument produced using a 2-μm period silicon grating. (a) Plot of the normalized spin-echo polarization against wavelength. The *n*th peak corresponds to a spin-echo length equal to *n* times the grating period. The wavelength and corresponding spin-echo length is extracted and plotted in the next panel (b). The quadratic fit is drawn in red.

which for our estimated value of a_2 is equal to -8.62×10^3 Å^{-1}. Since according to Eq. (23) ℓ_+ and ℓ_- are equal in magnitude, it follows that the OAM of each state scales with $\ell_\pm = \pm\frac{1}{2}c_{\mathrm{OAM}}\lambda$.

IV. RESULTS

The normalized polarization, for the positive $\pi/2$ rotator polarity, is shown in Fig. 6(a). This represents a typical spin-echo curve obtained from this experiment. It is clear that the raw data contains oscillations, which increase in amplitude with wavelength squared, analogous to the precession plane oscillation described in the previous section [see Eq. (38)]. By subtracting a quadratic fit from the data and dividing the result by λ^2, the oscillations can be isolated [see Fig. 6(b)]. It can be shown that the abberation consists of two oscillations with frequencies $k_2 \approx 2k_1$. As pointed out previously it is important to correct for these oscillations, since in addition to improving the overall fit quality, the amplitude information is necessary to correct for a systematic error coming from imperfections of the instrument; hence, both amplitudes are listed in Table I. The data is corrected by fitting two sine waves to the oscillations and subtracting said fit multiplied by λ^2 from the data. The corrected data for both $\pi/2$ coil settings is shown in Fig. 7. Quadratic fits using a weighted least-squares method are applied to the corrected data.

TABLE I. Table showing the second-order fit parameters a_2 and their respective standard deviations, for both coil polarities and the amplitudes of the oscillations found in the data with their respective errors. The final estimate for the second-order parameter owing to the Sagnac effect a_2^S, which is calculated using Eq. (40), is shown at the bottom, in addition to the OAM proportionality constant [see Eq. (39)].

	a_2 (Å^{-2}) × 10^3	$\lvert A_1\rvert$ (Å^{-2}) × 10^5	$\lvert A_2\rvert$ (Å^{-2}) × 10^5
P_+	-0.891 ± 0.0853	14.4 ± 2.31	8.22 ± 2.24
P_-	0.898 ± 0.0739	8.88 ± 1.85	6.23 ± 1.83
$a_2^S = (-0.894 \pm 0.0564) \times 10^{-3}$ Å^{-2}		$c_{\mathrm{OAM}} = -6767 \pm 427$ Å^{-1}	

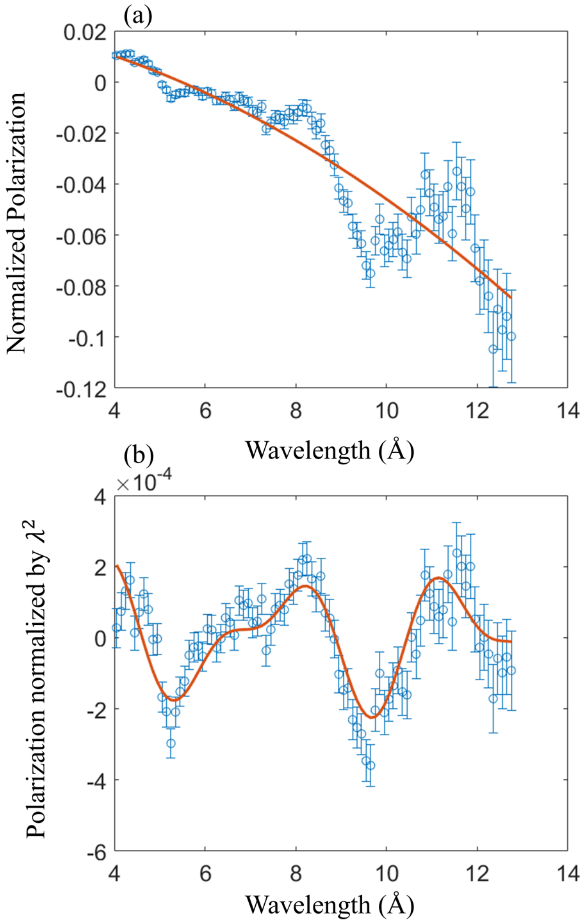

FIG. 6. (a) Typical normalized polarization for the 40 degree poleshoe setting, in which the Sagnac phase shift is expected (blue). A quadratic fit is shown in red. The quadratic fit can be subtracted from the data to isolate the oscillations. (b) Since the amplitude of the oscillations scale with wavelength squared, we divide these by λ^2. A fit consisting of two sines is shown in red.

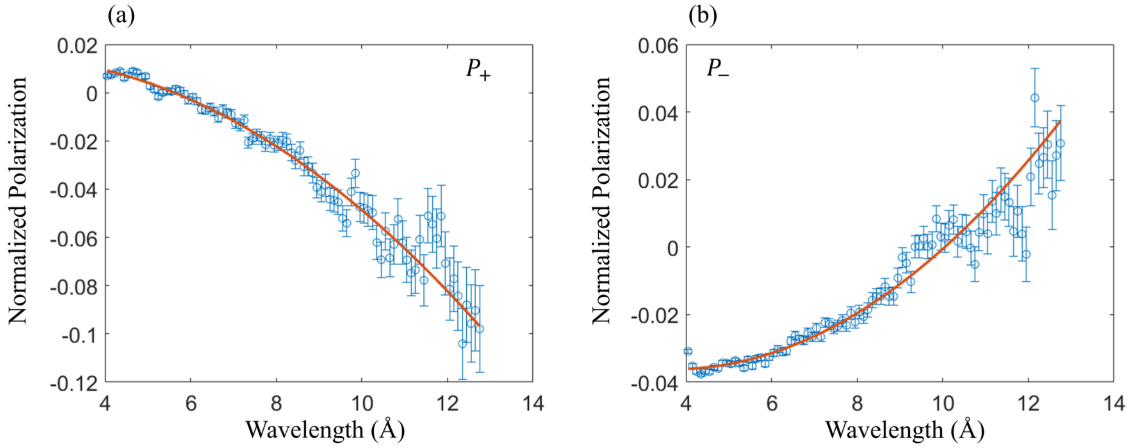

FIG. 7. Plots of the normalized and corrected polarization in blue for (a) positive polarity and (b) negative $\pi/2$ rotator polarity. The quadratic fits are plotted in red. The error bar introduced by subtracting the sinusoidal fit is negligible.

The weights are given by the inverted variance. The second-order fit parameters are illustrated in Table I. The first estimate for the second-order parameter a_2^S, owing to the Sagnac effect is obtained using the following:

$$a_2^S = \frac{a_2^+ - a_2^-}{2}. \tag{40}$$

Alternatively, the corrected data may be aggregated according to a similar formula

$$P_S = \frac{P_+ - P_-}{2} \tag{41}$$

and a weighted least-squares quadratic fit is applied to this result. P_S is shown in Fig. 8. The resulting second-order fit parameter is $(-0.899 \pm 0.0631) \times 10^{-3}$, which is in good agreement with the value a_2^S shown in Table I. For comparison, Fig. 8 shows a fit in green, which uses the theoretically exact value for the second-order parameter, while the zeroth- and first-order coefficients are determined via least-squares regression.

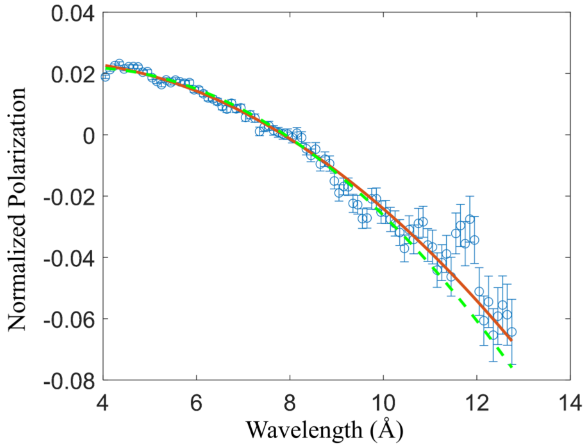

FIG. 8. Averaged-normalized polarization of all data, according to Eq. (41), shown in blue. The quadratic fit is shown as a red-solid line. While a fit containing the exact theoretical expectation value for the second-order term owing to the Sagnac effect is shown as a green-dashed line.

V. DISCUSSION

Figure 8 indicates a good agreement between our calculated Sagnac parameter of -1.15×10^{-3} Å^{-2} and the measured parameter; however, the exact fit parameters shown in Table I indicate that for a single $\pi/2$ rotator polarity the measured value differs from our calculation by roughly 3σ. Furthermore, the averaged fit parameter a_2^S differs from theory by 4.3σ, indicating a high likelihood of a systematic perturbation. In this section we correct this perturbation to the second-order fit parameter, assuming it is caused by imperfections in the adiabatic spin optical components. Both the oscillations shown in Fig. 6 and the large $\propto 4\sigma$ deviation between data indicate that such imperfections are likely. As indicated earlier at low efficiencies adiabatic spin-flip probabilities scale with λ^2, consistent with our observation. Therefore, we postulate that the oscillations shown in Fig. 6(b) arise owing to an oscillation of the precession plane of the form

$$P = 2\lambda^2[|A_1|\cos^2(k_1\lambda + \phi_1) + |A_2|\cos^2(k_2\lambda + \phi_2)], \tag{42}$$

similar to Eq. (38), which introduces a systematic to the second-order fit parameter of $\pm[|A_1| + |A_2|]$, where the sign is determined by the polarity of the $\pi/2$ rotator. The corrected second-order parameters $\bar{a}_2$ using the amplitudes in Table I are shown in Table II. After applying this correction the average estimated second-order parameter owing to the Sagnac effect is $(-1.083 \pm 0.078) \times 10^{-3}$, which is within 1σ of the expected theoretical value. This corresponds to an OAM proportionality constant of -8197 ± 590 units of $\hbar$/Å according to Eq. (39). From this the average OAM eigenvalues $\ell_\pm$ of the two path states can be extracted, $\ell_\pm = \pm 4098 \pm 295\hbar/\text{Å} \cdot \lambda$. This can be compared to the results of our calibration measurement (Fig. 5), which, based on Eq. (23), allows us to estimate the average OAM eigenvalue $\ell_\pm = \pm 4310$, which is within 1σ of the estimate achieved using the Sagnac effect. Two years ago in 2022, the first definitive observation of intrinsic longitudinal OAM was reported [15]. We now

TABLE II. Corrected estimates for the second-order parameter owing to the Sagnac effect $\bar{a}_2$ and their respective errors for both $\pi/2$ coil polarities and their average, in addition to the OAM proportionality constant $\bar{c}_{\mathrm{OAM}}$ for each setting. For comparison our theoretical estimate for a_2 is -1.15×10^{-3} Å^{-2} and for c_{OAM} is -8.62×10^3 Å^{-1}.

	$\bar{P}_+$	$\bar{P}_-$	$\frac{\bar{P}_+ - \bar{P}_-}{2}$
$\bar{a}_2(\text{Å}^{-2}) \times 10^3$	-1.117 ± 0.121	1.049 ± 0.098	-1.083 ± 0.078
$\bar{c}_{\mathrm{OAM}}(\text{Å}^{-1})$	-8454 ± 916	7940 ± 742	-8197 ± 590

conclude that the Sagnac effect represents the first definitive detection of transverse neutron OAM, since it depends only on the projection of the OAM on the axis of rotation [Eq. (21)], meaning that OAM must be present to explain a nonzero result.

Further, answering the criticism raised in [25], against the first experiments with neutron beam OAM [12], we propose to use OAM-rotation coupling to definitively detect longitudinal OAM. To accomplish this two technical difficulties need to be overcome: (i) the sensitivity of the technique needs to be increased; and (ii) the rotation axis should be more closely aligned with the beam axis to measure the longitudinal OAM component. The sensitivity of this method, using the earths rotation, is sufficient for detecting large quanta of OAM $|\ell| > 10^3$; however, it can be significantly improved by increasing the rotation frequency. A higher effective rotation frequency can be achieved by inserting a rotating dove mirror (see e.g., [14,27,52]) in the center of the instrument. Such devices are ubiquitous in photo-optics when it comes to measuring and sorting spin-orbit states [53,54]; hence, we expect them to be equally useful in neutron optics, should they be implemented. A pair of dove mirrors effectively rotate the image around the optical axis of the devices. A low rotation frequency of 1 Hz, would increase sensitivity by 10^5, compared to earths rotation. This method would increase a_2 and c_{OAM}, such that the systematic induced by the slight oscillations of the precession plane becomes insignificant, since both parameters are proportional to the rotation frequency Ω. In addition the dove prism would address the second difficulty as well, since the axis of rotation for such a device can be chosen arbitrarily, including parallel to the propagation direction. The dove mirror could be made compact, albeit monochromatic, if mosaic crystals are used to produce reflections. Intuitively one may come to the conclusion that the dove mirror technique would only work if the cross section of the dove mirror is of a similar size as the neutron coherence length, owing to the fact that a neutron propagating off-axis but parallel to optical axis of the dove mirror, in its own frame of reference is not only rotated around its propagation axis, but also translated on a circle around the optical axis of the dove mirror. However, intrinsic longitudinal OAM is translation invariant. In addition, we have shown that the Sagnac method measures the OAM difference between two states, which is translation invariant. As a result, we conclude that the ratio between the cross section of the mirror and the neutron coherence length is irrelevant to the success of this technique. Instead, in SESANS interferometers it is important that the optical axis of the dove mirrors is precisely aligned with the optical axis of the interferometer. SESANS is designed to measure ultra small angle scattering; hence, the alignment precision must exceed the instrument resolution. Luckily the resolution is proportional to the spin-echo length $q_{\min} \propto \frac{1}{\delta_{SE}}$ and Fig. 4 demonstrates that a low spin-echo length produces an optimal superposition of $\ell = \pm 1$. Thus, for a typical thermal neutron beam the alignment of the dove prism must be to within $0.1 - 1$ degree of the optical axis of the interferometer, so as to not introduce artifacts. We postulate that dove mirrors will play an important role in neutron OAM optics for OAM manipulation and detection, since as opposed to the scattering methods reported on in [17–19], which depend on still unknown matrix elements, the efficiency of a Sagnac-based method is independent of other attributes of the neutron wavepacket such as transverse momentum and coherence length. In addition the Sagnac method ought to provide a faster method than the interferometric methods used in, e.g., [15,24], since these approaches require detectors with spatial resolution to resolve the OAM phase structure. Because of the low flux of neutron beams this requirement of spatial or angular resolution results in a larger integration time compared to the Sagnac method. Since the matrix elements, which determine the scattering amplitudes of twisted neutrons from nuclei are still unknown, the Sagnac method may be used to calibrate twisted scattering techniques. (Dove) mirrors may also be used to increase the sensitivity of our measurement to extrinsic transverse OAM. A mirror at the center of our instrument rotating around the vertical of the instrument effectively acts as a rotation of the instrument. As a result one can simulate faster rotating frequencies than that provided by the earth.

As pointed out in previous sections our technique uses spin-orbit entanglement to imprint OAM-dependent phases on the spin [see e.g., Eq. (24)] and to characterize these phases by measuring the spin projection. This is somewhat analogous to the entangled optical interferometer reported on in [55], which makes use of interparticle entanglement, while we report on intraparticle or mode entanglement. The 1σ precision achieved in our experiment corresponds to a rotational sensitivity of 5.1 μrad s^{-1}, similar to what is reported in [55], which to our our knowledge is the most sensitive measurement of the Sagnac effect using entanglement.

ACKNOWLEDGMENTS

N.G. and S.S. acknowledge funding from the Austrian Science Fund (FWF), Project No. P34239. N.G. and W.M.S. are supported by the US Department of Energy (DOE) Grant No. DE-SC0023695. W.M.S. and K.S. acknowledge support from the US National Science Foundation (NSF) Grant No. PHY-2209481 and the Indiana University Center for Spacetime Symmetries. The authors extend their gratitude to Gøran Nilsen for supplying the ramped $\pi/2$ flipper. Experiments at the ISIS Neutron and Muon Source were supported by a beamtime allocation RB2410116 [43] from the Science and Technology Facilities Council.

[1] M. G. Sagnac, The demonstration of the luminiferous aether by an interferometer in uniform rotation, Comptes Rendus **157**, 708 (1913).

[2] E. J. Post, Sagnac effect, Rev. Mod. Phys. **39**, 475 (1967).

[3] A. A. Michelson, H. G. Gale, and F. Pearson, The effect of the earth's rotation on the velocity of light, II, Astrophys. J. **61**, 140 (1925).

[4] J. E. Zimmerman and J. E. Mercereau, Compton wavelength of superconducting electrons, Phys. Rev. Lett. **14**, 887 (1965).

[5] S. A. Werner, J. L. Staudenmann, and R. Colella, Effect of earth's rotation on the quantum mechanical phase of the neutron, Phys. Rev. Lett. **42**, 1103 (1979).

[6] F. Hasselbach and M. Nicklaus, Sagnac experiment with electrons: Observation of the rotational phase shift of electron waves in vacuum, Phys. Rev. A **48**, 152 (1993).

[7] F. Riehle, Th. Kisters, A. Witte, J. Helmcke, and Ch. J. Bordé, Optical Ramsey spectroscopy in a rotating frame: Sagnac effect in a matter-wave interferometer, Phys. Rev. Lett. **67**, 177 (1991).

[8] R. Gautier, M. Guessoum, L. A. Sidorenkov, Q. Bouton, A. Landragin, and R. Geiger, Accurate measurement of the Sagnac effect for matter waves, Sci. Adv. **8**, eabn8009 (2022).

[9] B. Mashhoon, Neutron interferometry in a rotating frame of reference, Phys. Rev. Lett. **61**, 2639 (1988).

[10] B. Demirel, S. Sponar, and Y. Hasegawa, Measurement of the spin–rotation coupling in neutron polarimetry, New J. Phys. **17**, 023065 (2015).

[11] A. Danner, B. Demirel, W. Kersten, H. Lemmel, R. Wagner, S. Sponar, and Y. Hasegawa, Spin-rotation coupling observed in neutron interferometry, npj Quantum Inf. **6**, 23 (2020).

[12] C. W. Clark, R. Barankov, M. G. Huber, M. Arif, D. G. Cory, and D. A. Pushin, Controlling neutron orbital angular momentum, Nature (London) **525**, 504 (2015).

[13] D. Sarenac, C. Kapahi, W. Chen, C. W. Clark, D. G. Cory, M. G. Huber, I. Taminiau, K. Zhernenkov, and D. A. Pushin, Generation and detection of spin-orbit coupled neutron beams, Proc. Natl. Acad. Sci. USA **116**, 20328 (2019).

[14] N. Geerits and S. Sponar, Twisting neutral particles with electric fields, Phys. Rev. A **103**, 022205 (2021).

[15] D. Sarenac, M. E. Henderson, H. Ekinci, C. W. Clark, D. G. Cory, L. DeBeer-Schmitt, M. G. Huber, C. Kapahi, and D. A. Pushin, Experimental realization of neutron helical waves, Sci. Adv. **8**, eadd2002 (2022).

[16] Z. W. Lu, L. Guo, Z. Z. Li, M. Ababekri, F. Q. Chen, C. Fu, C. Lv, R. Xu, X. Kong, Y. F. Niu, and J. X. Li, Manipulation of giant multipole resonances via vortex γ photons, Phys. Rev. Lett. **131**, 202502 (2023).

[17] A. V. Afanasev, D. V. Karlovets, and V. G. Serbo, Schwinger scattering of twisted neutrons by nuclei, Phys. Rev. C **100**, 051601(R) (2019).

[18] A. V. Afanasev, D. V. Karlovets, and V. G. Serbo, Elastic scattering of twisted neutrons by nuclei, Phys. Rev. C **103**, 054612 (2021).

[19] T. Jach and J. Vinson, Method for the definitive detection of orbital angular momentum states in neutrons by spin-polarized ^{3}He, Phys. Rev. C **105**, L061601 (2022).

[20] F. C. Michel, Parity nonconservation in nuclei, Phys. Rev. **133**, B329 (1964).

[21] T. Giordani, E. Polino, S. Emiliani, A. Suprano, L. Innocenti, H. Majury, L. Marrucci, M. Paternostro, A. Ferraro, N. Spagnolo, and F. Sciarrino, Experimental engineering of arbitrary qudit states with discrete-time quantum walks, Phys. Rev. Lett. **122**, 020503 (2019).

[22] M. V. Berry, Paraxial beams of spinning light, Proc. SPIE **3487**, 6 (1998).

[23] A. T. O'Neil, I. MacVicar, L. Allen, and M. J. Padgett, Intrinsic and extrinsic nature of the orbital angular momentum of a light beam, Phys. Rev. Lett. **88**, 053601 (2002).

[24] N. Geerits, H. Lemmel, A. Berger, and S. Sponar, Phase vortex lattices in neutron interferometry, Nat. Comm. Phys **6**, 209 (2023).

[25] R. Cappelletti, T. Jach, and J. Vinson, Intrinsic orbital angular momentum states of neutrons, Phys. Rev. Lett. **120**, 090402 (2018).

[26] W. Treimer, F. Haußer, and M. Suda, Computerized simulation of 2-dimensional phase contrast images using spiral phase plates in neutron interferometry, Z. Naturforsch **79**, 873 (2024).

[27] J. Courtial, K. Dholakia, D. A. Robertson, L. Allen, and M. J. Padgett, Measurement of the rotational frequency shift imparted to a rotating light beam possessing orbital angular momentum, Phys. Rev. Lett. **80**, 3217 (1998).

[28] H. Rauch, H. Wolwitsch, H. Kaiser, R. Clothier, and S. A. Werner, Measurement and characterization of the three-dimensional coherence function in neutron interferometry, Phys. Rev. A **53**, 902 (1996).

[29] A. G. Wagh, S. Abbas, and W. Treimer, The plain truth about forming a plane wave of neutrons, Nucl. Instrum. Methods Phys. Res. Sect. A **634**, S41 (2011).

[30] S. McKay, A. A. M. Irfan, Q. Le Thien, N. Geerits, S. R. Parnell, R. M. Dalgliesh, N. V. Lavrik, I. I. Kravchenko, G. Ortiz, and R. Pynn, Experimental evidence for the two-path description of neutron spin echo, Phys. Rev. A **109**, 042420 (2024).

[31] R. Gaehler, R. Golub, K. Habicht, T. Keller, and J. Felber, Space-time description of neutron spin echo spectrometry, Phys. B **229**, 1 (1996).

[32] W. G. Bouwman, C. P. Duif, J. Plomp, A. Wiedenmann, and R. Gahler, Combined SANS-SESANS, from 1 nm to 0.1 mm in one instrument, Phys. B **406**, 2357 (2011).

[33] N. Geerits, S. R. Parnell, M. A. Thijs, A. A. van Well, C. Franz, A. L. Washington, D. Raspon, R. M. Dalgliesh, and J. Plomp, Time of flight modulation of intensity by Zero effort, Rev. Sci. Inst. **90**, 125101 (2019).

[34] J. Shen, S. J. Kuhn, R. M. Dalgliesh, V. O. de Haan, N. Geerits, A. A. M. Irfan, F. Li, S. Lu, S. R. Parnell, J. Plomp *et al.*, Unveiling contextual realities by microscopically entangling a neutron, Nat. Commun. **11**, 930 (2020).

[35] S. J. Kuhn, S. McKay, J. Shen, N. Geerits, R. M. Dalgliesh, E. Dees, A. A. M. Irfan, F. Li, S. Lu, V. Vangelista, D. V. Baxter, G. Ortiz, S. R. Parnell, W. M. Snow, and R. Pynn, Neutron-state entanglement with overlapping paths, Phys. Rev. Res. **3**, 023227 (2021).

[36] Y. Hasegawa, R. Loidl, G. Badurek, K. Durstberger-Rennhofer, S. Sponar, and H. Rauch, Engineering of triply entangled states in a single-neutron system, Phys. Rev. A **81**, 032121 (2010).

[37] K. Y. Bliokh and F. Nori, Transverse and longitudinal angular momenta of light, Phys. Rep. **592**, 1 (2015).

[38] M. Abramowitz and I. Stegun, *Handbook of Mathematical Functions with Formulas, Graphs, and Mathematical Tables* (Cambridge University Press, Cambridge, 1964).

[39] G. N. Watson, *A Treatise on the Theory of Bessel Functions* (Cambridge University Press, Cambridge, 1944).

[40] H. Bateman, *Tabels of Integral Transforms* (McGraw-Hill, New York, 1954), Vol. B.

[41] R. Cappelletti and J. Vinson, Photons, orbital angular momentum, and neutrons, Phys. Status Solidi (b) **258**, 2000257 (2021).

[42] V.-O. de Haan, J. Plomp, A. A. van Well, M. Theo Rekveldt, Y. H. Hasegawa, R. M. Dalgliesh, and N.-J. Steinke, Measurement of gravitation-induced quantum interference for neutrons in a spin-echo spectrometer, Phys. Rev. A **89**, 063611 (2014).

[43] R. Dalgliesh, M. Snow, V. de Haan, K. Steffen, and N. Geerits, Detection of the Sagnac effect in SESANS (2024), https://doi.org/10.5286/ISIS.E.RB2410116.

[44] M. T. Rekveldt, Novel sans instrument using neutron spin echo, Nucl. Instrum. Methods Phys. Res. Sect. B **114**, 366 (1996).

[45] F. Li, S. R. Parnell, H. Bai, W. Yang, W. A. Hamilton, B. B. Maranville, R. Ashkar, D. V. Baxter, J. Ted Cremer, and R. Pynn, Spin echo modulated small-angle neutron scattering using superconducting magnetic wollaston prisms, J. Appl. Crystallogr. **49**, 55 (2016).

[46] S. R. Parnell, A. A. van Well, J. Plomp, R. M. Dalgliesh, N.-J. Steinke, J. F. K. Cooper, K. E. Steffen N. Geerits, W. M. Snow, and V. O. de Haan, Search for exotic spin-dependent couplings of the neutron with matter using spin-echo based neutron interferometry, Phys. Rev. D **101**, 122002 (2020).

[47] G. J. Nilsen, J. Kosata, M. Devonport, P. Galsworthy, R. I. Bewley, D. J. Voneshen, R. Dalgliesh, and J. R. Stewart, Polarisation analysis on the let time-of-flight spectrometer, J. Phys.: Conf. Ser. **862**, 012019 (2017).

[48] G. Cassella, J. R. Stewart, G. M. Patern, V. Garcia Sakai, M. Devonport, P. J. Galsworthy, R. I. Bewley, D. J. Voneshen, D. Raspino, and G. J. Nilsen, Polarization analysis on the LET cold neutron spectrometer using a ^{3}He spin-filter: First results, J. Phys.: Conf. Ser. **1316**, 012007 (2019).

[49] S. Lu, Abu Ashik Md. Irfan, J. Shen, S. J. Kuhn, W. Michael Snow, D. V. Baxter, R. Pynn, and G. Ortiz, Operator analysis of contextuality-witness measurements for multimode-entangled single-neutron interferometry, Phys. Rev. A **101**, 042318 (2020).

[50] S. V. Grigoriev, R. Kreuger, W. H. Kraan, F. M. Mulder, and M. T. Rekveldt, Neutron wave-interference experiments with adiabatic passage of neutron spin through resonant coils, Phys. Rev. A **64**, 013614 (2001).

[51] W. H. Kraan, S. V. Grigoriev, M. Th. Rekveldt, H. Fredrikze, C. F. de Vroege, and J. Plomp, Test of adiabatic spin flippers for application at pulsed neutron sources, Nucl. Instrum. Methods Phys. Res. Sect. A **510**, 334 (2003).

[52] J. Leach, M. J. Padgett, S. M. Barnett, S. Franke-Arnold, and J. Courtial, Measuring the orbital angular momentum of a single photon, Phys. Rev. Lett. **88**, 257901 (2002).

[53] S. Slussarenko, V. D'Ambrosio, B. Piccirillo, L. Marrucci, and E. Santamato, The polarizing Sagnac interferometer: A tool for light orbital angular momentum sorting and spin-orbit photon processing, Opt. Express **18**, 27205 (2010).

[54] F. X. Wang, W. Chen, Y. P. Li, G. W. Zhang, Z. Q. Yin, S. Wang, G. C. Guo, and Z. F. Han, Single-path Sagnac interferometer with dove prism for orbital-angular-momentum photon manipulation, Opt. Express **25**, 24946 (2017).

[55] R. Silvestri, H. Yu, T. Strömberg, C. Hilweg, R. W. Peterson, and P. Walther, Experimental observation of earth's rotation with quantum entanglement, Sci. Adv. **10**, eado0215 (2024).